Unveiling the mechanism of phase and morphology selections during the devitrification of Al-Sm amorphous ribbon

Fanqiang Meng, Yang Sun, Feng Zhang, Bo Da, Cai-Zhuang Wang, Matthew J. Kramer, Kai-Ming Ho, and Dongbai Sun

Phys. Rev. Materials **5**, 043402 — Published 19 April 2021
DOI: 10.1103/PhysRevMaterials.5.043402

Unveiling the mechanism of phase and morphology selections during the devitrification of Al-Sm amorphous ribbon

Fangqiang Meng[1], Yang Sun[2,3*], Feng Zhang[2], Bo Da[4], Cai-Zhuang Wang[2], Matthew J. Kramer[2], Kai-Ming Ho[2], Dongbai Sun[1,5*]

---

[*] Email: ys3339@columbia.edu (YS) or sundongbai@mail.sysu.edu.cn (DS)

[1]Sino-French Institute of Nuclear Engineering and Technology, Sun Yat-Sen University, Zhuhai, Guangdong, 519082, China
[2]Ames Laboratory, U.S. Department of Energy and Department of Physics, Iowa State University, Ames, Iowa 50011, USA
[3]Department of Applied Physics and Applied Mathematics, Columbia University, New York, New York 10027, USA
[4]Research and Services Division of Materials Data and Integrated System, National Institute for Materials Science, 1-1 Namiki, Tsukuba, Ibaraki 305-0044, Japan
[5]School of Materials, Sun Yat-Sen University, Guangzhou, Guangdong, 510275, China

Abstract

The complex interplay between energetic and kinetic factors that governs the phase and morphology selections can originate at the earliest stage of crystallization in the amorphous parent phases. Because of the extreme difficulties in capturing the microscopic nucleation process, a detailed picture of how initial disordered structures affect the transformation pathway remains unclear. Here, we report the experimental observation of widely varying phase selection and grain size evolution during the devitrification of a homogeneous melt-spun glassy ribbon. Two different crystalline phases, θ-Al_5Sm and ε-$Al_{60}Sm_{11}$, are found to form in the different regions of the same metallic glass ribbon during the devitrification. The grain size of ε-$Al_{60}Sm_{11}$ phase shows a strong spatial heterogeneity. Coarse-grained ε-$Al_{60}Sm_{11}$ phase coupled with the small volume fraction of θ-Al_5Sm phase is preferably formed close to wheel side of the melt-spun ribbon. Combining experimental characterization and computational simulations, we show that phase selection and microstructure evolution can be traced back to different types and populations of atomic clusters that serve as precursors for the nucleation of different crystalline phases. Inhomogeneous cooling rates cause different structure orders across the glass sample during the quenching process. Our findings provide direct insight into the effect of structural order on the crystallization pathways during the devitrification of metallic glass. It also opens an avenue to study the detailed nucleation process at the atomic level using the metallic glass as a platform and suggests the opportunity of microstructure and property design via controlling the cooling process.

1. Introduction

Understanding crystallization pathways plays a key role in discovering and designing new materials[1]. When a liquid is cooled slowly, phase selection typically follows the equilibrium phase diagram. With deeper undercooling, solidification rates increase, driving the system further from equilibrium. Under very high cooling rates, crystallization can be frustrated, and glass can form. Devitrification by reheating glass systems can have an asymmetric behavior in the phase selection compared to the crystallization by cooling from the liquid, emphasizing the complex competition between thermodynamics and kinetics [2,3]. Solidification or devitrification under far-from-equilibrium conditions can often lead to unexpected phase selection and microstructures[4-6], which is of vital importance in the design of materials with tailored structures and properties. Understanding its fundamental physics of transformation pathways by which different microstructures evolve as a function of increasing departure from equilibrium is essential. However, observing the atomic-level process of nucleation from the very beginning of crystallization remains to be a long-time challenge [7-10].

As a representative far-from-equilibrium system, *glass*, sometimes thought of as a "frozen liquid" state [11], provides an ideal platform to investigate the correlation between pre-existing nuclei retained during the vitrification and phase transformation pathway in the devitrification process. Even the structurally simplest metallic glass (MG) has shown a far-richer-than-expected phase transformation behaviors[12-14]. Phase selection during devitrification is not only affected by the thermodynamic driving force but also kinetic factors. Several scenarios were proposed to understand the crystallization of amorphous materials, e.g. phase separation [15-17] and diffusion-controlled nucleation [18]. Recent studies of atomic structure evidence that structural ordering can be quite abundant in the seemly homogeneous liquids and glasses[19-23]. Local clusters from undercooled melts or amorphous alloys, such as icosahedral clusters [24,25], quenched-in nuclei [26] [27], short- and medium-range order [24,28], are believed to have an impact on subsequent crystallization and devitrification. It was proposed [27] that structural similarities between the crystalline phase and quenched-in nuclei can reduce the interfacial energy, and thus, promote polymorphic devitrification processes. Detailed analysis of theoretical models also indicates competing orders between the crystalline phase and liquids can impact the crystal-forming and glass-forming behavior [29]. Therefore, it requires detailed information on structural orders in the initial liquid and glass states to understand the phase selection and microstructure in the subsequent crystallization and devitrification processes.

In this work, we focus on Al-Sm MG, which has complex phase selections during devitrification. A small variation of Sm concentration can significantly alter the devitrification mechanisms of amorphous Al-Sm alloys, which varies from primary crystallization of nano-scaled α-Al at 8at%Sm, polymorphic transformation at 10at%Sm, and eutectic crystallization for 12at%Sm [30]. Recent experiments coupled with computer simulations suggested the complex metastable phase selection in Al-Sm are dependent on chemical composition and the processing technique, such as melting-spinning [14], magnetron sputtering [13] or solid-state amorphization

[31]. The AlSm MG of melt-spun ribbon (MSR) can devitrify into the ε-$Al_{60}Sm_{11}$ crystalline phase [14], while the θ-Al_5Sm phase was found to crystallize from the AlSm MG of sputtered thin film (STF) [13]. Computer simulations revealed that the devitrified crystalline phases exhibit similar atomic clusters with the undercooled AlSm liquids [32]. It was also found the anisotropy of crystal growth of Al-Sm alloy has a strong correlation with atomic interfacial structures [33].

In the present study, we analyzed the initial crystallization and the grain size of the phases devitrified from the binary Al-Sm glassy ribbon. We show a strong dependence of phase selection and morphology on the distance from the wheel side surface in the melt spinning. Coarse-grained ε-$Al_{60}Sm_{11}$ coupled with a small volume fraction of θ-Al_5Sm phases are present close to the wheel side of the ribbon, where the highest cooling rate is achieved. Meanwhile, ε-$Al_{60}Sm_{11}$ phase with smallest grain size locates around 5 μm away from the wheel side. With the help of computer simulation, we rationalize the interdependence of the phase selection during devitrification and the local cooling rate during vitrification.

2. Method

2.1 Experimental procedures

Al-12.4at%Sm ingot was prepared by Materials Preparation Center (MPC, Ames Laboratory (USDOE) [34]) by arc melting 99.9%Sm and 99.99%Al in an argon atmosphere. Amorphous ribbons with an average thickness of ~20 μm were produced by a single copper block melt-spinner, quenching from 1373 K at a tangential wheel speed of 30m/s. The ejection pressure used is 120 ± 1 torr He over the base chamber pressure [35]. The amorphous nature of the ribbon was confirmed using TEM, lab-source X-ray diffraction (XRD, Bruker D8 Discover diffractometer with Cu target) and high energy synchrotron X-ray scattering. The representative TEM image with corresponding SAD and WAXS pattern shown in Supplementary Materials (Ref. []) reveals the only amorphous phase without any crystal. The chemical composition of the melt-spun ribbon was measured using X-ray fluorescence (Bruker Tornado M4) and energy-dispersive X-ray spectroscopy (EDS) equipped on a scanning electronic microscope (FEI Teno Lovac). The crystallization behaviors of the as-spun amorphous ribbons were characterized using dynamic scanning calorimetry (DSC, Perkin Elmer Pyris 1) with a constant heating rate of 10 K/min.

The devitrification during isochronal heating was examined in situ using time-resolved high energy X-ray diffraction, utilizing monochromatic X-rays (energy of 71.77kev, the wavelength of 0.01729nm) at the sector 1-ID-E of Advanced Photon Source (APS) at Argonne

National Laboratory operated by the U.S. Department of Energy. A two-stage forward-scattering detector configuration was used for simultaneous collection of Wide-Angle (WAXS) and Small Angle X-ray Scattering (SAXS) signals. Samples used for WAXS/SAXS experiments were filled in a thin-walled SiO_2 capillary tube with 2mm inner diameter and sealed in argon. For in-situ heating, the capillary was placed in a tubular stainless-steel holder with a 5 mm x-ray pass window, which was heated using an infrared furnace. Two thermocouples were placed in contact with the capillary to record temperatures. The measured temperatures for the furnace used at APS were calibrated to the temperatures measured via DSC run using at identical heating rates.

The microstructure evolution during devitrification was further probed using transmission electron microscopy (TEM) and scanning transmission electron microscope (STEM). Samples for TEM/STEM characterization were prepared using a dual-beam focused ion beam instrument (FEI Helios NanoLab G3 UC). The observations were carried out using Tecnai G^2 F20 and FEI Titan Themis 300 Cubes aberration-corrected instruments equipped with an EDS detector at an operation voltage of 200 kV.

2.2 Computational methods

The long-time, large scale MD simulation was performed using the GPU-accelerated LAMMPS [36-38] code with a semi-empirical potential [39] in the Finnis-Sinclair form [40] for the energy calculations. The MG structures from this potential have been demonstrated good agreement with the structure of $Al_{90}Sm_{10}$ liquid determined from *ab initio* MD simulations and amorphous solids in experiments[32]. The constant number of atoms, pressure, and temperature (NPT) ensemble is applied with Nose-Hoover thermostats. The time step of the simulation is 2.5 *fs*. A sub-Tg annealing technique [41] is employed to obtain the glass model with lower cooling rates. The initial liquid structure, containing 4500 Al atoms and 500 Sm atoms, are held at 2000K for 2.5 ns to reach equilibrium. Then the liquid is continuously cooled down with a constant cooling rate of 10^{10} K/s to 650 K, which is below the glass transition temperature $T_g \sim 693$ K [39]. After that, the as-quenched structure is annealed isothermally at 650 K for up to 50 μs, followed by a continuous cooling at 10^{10} K/s to 300K. Moreover, six other $Al_{90}Sm_{10}$ glass models were generated using uniform continuous cooling from 2000 K to 300 K with different cooling rates of 10^{13}, 10^{12}, 10^{11}, 10^{10}, $10^{9,}$ and 10^{8} K/s, respectively. The effective cooling rate of the sub-T_g annealed model is determined by the potential energy [42] as 4×10^{7} K/s.

3. Results and discussion

3.1 Dependence of phase selection and microstructure on the distance to the wheel side

Figure 1a shows the crystallization behaviors monitored using Dynamic Scanning Calorimetry (DSC) and *in-situ* synchrotron wide-angle X-ray scattering (WAXS) at a constant heating rate of 10 K/min. A two-stage phase transformations can be seen from the contrast changes in the WAXS patterns accompanied by two exothermic peaks in the DSC profile. Rietveld analysis (General Structure Analysis System (GSAS) software) was carried out to confirm the phase transformation sequences and evolution of phase fraction (see Fig. S2 in Supplementary Materials at Ref. []). The first exothermic peak is corresponding to the formation of the ε-$Al_{60}Sm_{11}$ phase, a cubic structure with a large unit cell containing 144 atoms and a=b=c=1.39 nm[14]. Continuous heating up to 538 K leads to the decomposition of ε-$Al_{60}Sm_{11}$ into π-Al_5Sm and *fcc*-Al (see Fig. S3 in Supplementary Materials at Ref. []). The representative Rietveld diffraction pattern at 500 K is shown in Fig. 1b, in which all the peaks can be indexed by the ε-$Al_{60}Sm_{11}$ phase with partial occupancy. Meanwhile, a diffuse halo is present at $2\theta=4.2^\circ$ in Fig.1b, suggesting the presence of an amorphous phase. *Ex-situ* TEM (Transmission Electron Microscopy) were employed to characterize the microstructural evolution. A bright-field TEM (BF-TEM) image of the ribbon heated at 10 K/min to 500 K and then cooled in a DSC furnace is shown in Fig. 1c. Well-defined grains with sizes varying by several hundred nanometers are observed in the region away from the wheel side surface. In contrast, the part closer to the wheel side surface appears to be still in amorphous nature, which is confirmed by the selected area diffraction (SAD, inset of Fig. 1c) pattern, consistent with the WAXS result. A clear interface between amorphous and ε-$Al_{60}Sm_{11}$ phases can be observed in the high-resolution TEM (High-Resolution TEM) image shown in Fig. 1d, suggesting the crystallization is not initiated close to the wheel side. The absence of nano-sized *fcc*-Al inside current ε-$Al_{60}Sm_{11}$ grains is different from the previously observed mixture of *fcc*-Al and ε-$Al_{60}Sm_{11}$ structures devitrified from AlSm MG with lower Sm concentrations[43,44]. It indicates the current devitrification may be in a partition-less manner. To further confirm its chemical homogeneity, the chemical composition is examined using energy dispersive spectrometer (EDS) measurement along the line indicated in Fig. 1c. Indeed, Fig. 1e shows the measured Al-Sm concentrations from the retained amorphous layer to crystalline grains do not present any chemical variation. Therefore, the crystallization from the current AlSm MG near the spinning wheel side has a spatial inhomogeneity with the coexistence of multiple ε-$Al_{60}Sm_{11}$ grains and amorphous, meanwhile shows a chemical homogeneity.

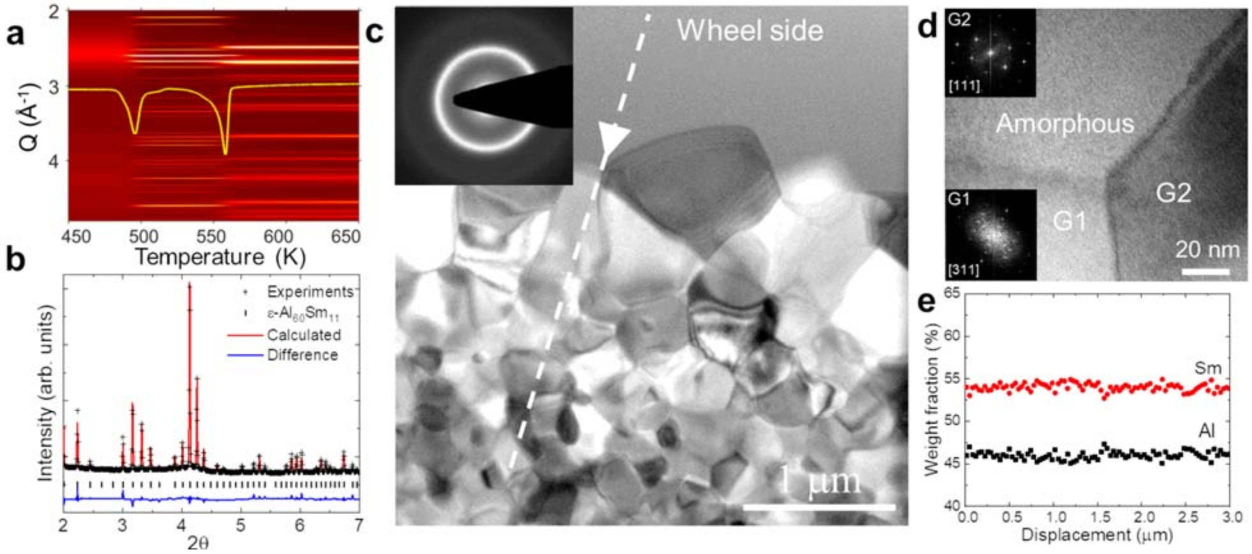

Fig. 1. Phase transformation and microstructure of AlSm MG upon devitrification. (a) Accumulated WAXS patterns as a function of temperature with a constant heating rate of 10ºC/min and corresponding DSC curve. (b) GSAS Rietveld result of WAXS pattern at a temperature of 500 K. (c) BF-TEM images of melt-spun ribbon after heating to 500 K in the DSC. The SAD pattern (inset) is obtained from the amorphous region close to the wheel side. The arrow indicates the direction away from the wheel side. (d) HR-TEM image of the interface between ε-$Al_{60}Sm_{11}$ and amorphous phases; FFT patterns (inset) from two different grains. (e) EDS element profiles along the dashed line marked in (c).

To further elucidate the crystallization behavior of the Al-Sm MSR, the devitrified sample is isothermally annealed at elevated 508 K for 720 s to characterize the morphology of crystallized phases. A representative TEM micrograph of the structure near the wheel side after isothermal annealing is shown in Fig. 2a. The amorphous layer close to the wheel side (Fig. 1c) no longer presents after the extended annealing at the elevated temperature. Instead, the structure becomes elongated and coarse grains, which then transit to finer grains with increasing distance from the wheel side surface. SAD patterns (not shown) for the grains demonstrate that most of the elongated grains are ε-$Al_{60}Sm_{11}$ phase except the region marked by the dashed line in Fig. 2a. The high angle annular dark-field scanning TEM (HAADF-STEM) image of the area close to the wheel side at higher magnification is shown in Fig. 2b, in which the chemical composition contrast is present, suggesting a multi-phase configuration. The high-resolution HAADF-STEM image and corresponding FFT patterns of regions A and B are shown in Fig. 2c and 2d, respectively. Fig. 2c shows the atomic structure in the ε-$Al_{60}Sm_{11}$ phase along with a superimposed schematic of the atomic packing. Due to the large *Z* contrast between Al and Sm atoms, Al sites are almost not visible in HAADF-STEM mode. The bright dots are mainly caused by the Sm sites [45], which is consistent with the lattices shown in the inset of Fig. 2c and 2d. The atomic packing in the B region (Fig. 2d) exhibits another structural pattern that is corresponding to the θ-Al_5Sm phase, which was observed only from Al-Sm sputtered thin-film previously[13]. The dark contrast in Fig. 2d is confirmed to be the *fcc*-Al distributed along the <001> direction of θ-Al_5Sm phase using high-resolution TEM.

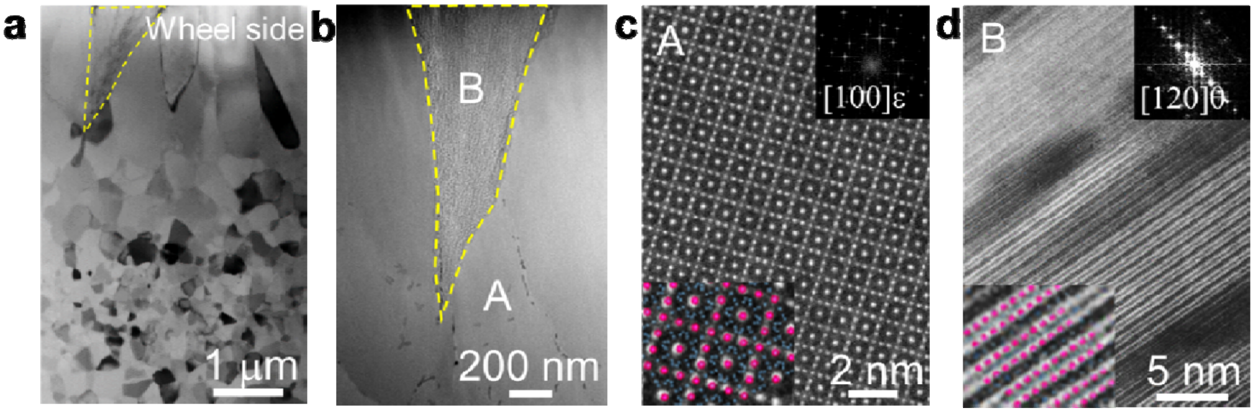

Fig. 2. Dependence of phase selection on the distance from the wheel side of a fully crystallized sample. (a) BF-TEM images of MSR annealed at 508K for 720s. The arrow indicates the direction away from the wheel side. (b) HAADF-STEM images of the region marked by the dashed line in (a). (c) and (d) are high-resolution HAADF-STEM images of ε-$Al_{60}Sm_{11}$ and θ-Al_5Sm phases corresponding to A and B regions in b, respectively. The insets are FFT pattern and superposed atomic structures with the patterns where red dots represent Sm, and blue dots are Al.

Not only is the phase selection dependent on relative distance from the wheel side surface, but the morphology of ε-$Al_{60}Sm_{11}$ grains is also dependent on this distance, as can be seen in Fig. 1c and Fig. 2a. The evolution of grain size as a distance from the wheel side was further examined by isothermally annealing a sample at different temperatures and times. The microstructure of the sample annealed at 478 K for 660 s is shown in Fig. 3a. Some amorphous regions are still retained in the area closest to the wheel side for this sample. In Fig. 3b, the grain sizes of the ε-$Al_{60}Sm_{11}$ phase are measured as a function of distance from the wheel side for samples annealed at both 478 K for 660 s (partial crystallized) and 508 K for 720 s (fully crystallized) using liner intercept method. Two independent samples were annealed at 478 K for 660 s to confirm the consistency in measurements. The grain size of the ε-$Al_{60}Sm_{11}$ phase is larger at the region closes to the wheel side and decreases with the increasing distance from the wheel side until reaching a minimum at ~ 4-5.5 μm away from the wheel side. With further increasing distance from the wheel side, the grain size increases again. Three samples show a very consistent trend of the grain size change as a function of distance from wheel sides.

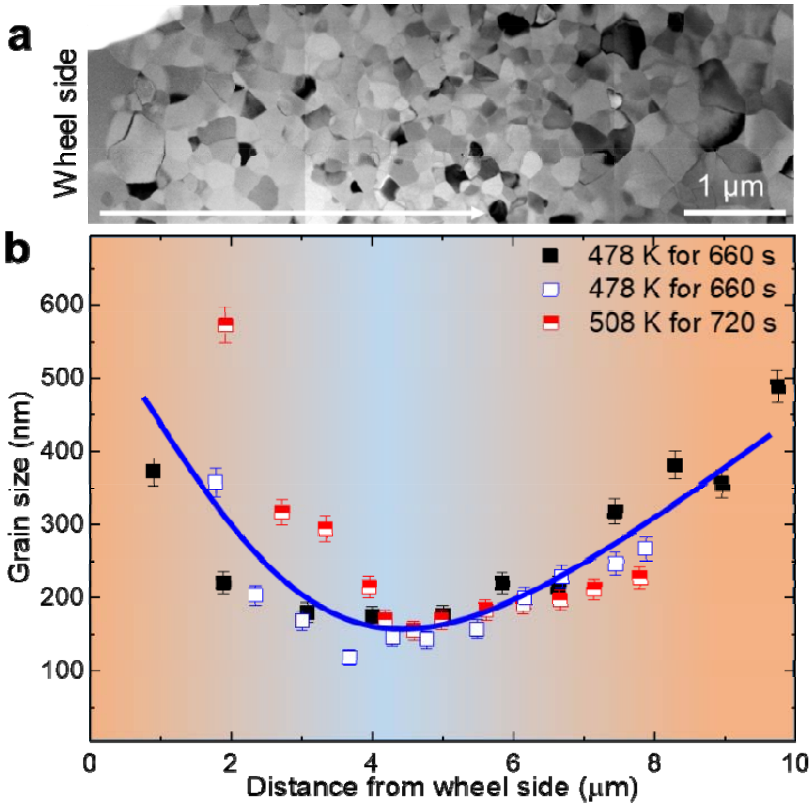

Fig. 3. Dependence of grain size on the distance from wheel-side to free side. (a) BF-TEM images of MSR sample annealed at 478 K for 660 s, in which minor amorphous phase is retained close to the wheel side. The arrow indicates the direction away from the wheel side. (b) Grain size as a function of distance to wheel side surface in three samples: two samples were partially crystallized at 478 K for 660 s, and one sample was fully crystallized at 508 K for 720 s; blue cures in is a guide-to-eye.

Current experiments show the phase selection and microstructural evolution during the devitrification of the Al-Sm MSR with a strong dependence on the distance from the wheel side surface. Fig. 1 indicates an inhomogeneous nuclei density of ε-$Al_{60}Sm_{11}$ phase from the wheel side to the free side in the MSR sample. This phenomenon should be attributed to the fact that the local cooling rate during the melt spinning varies significantly with the distance to the wheel side surface. Melts that are first spun to the wheel side surface should suffer the fastest cooling. Indeed, numerical modelings [46,47] suggest the cooling rate close to the wheel side at 30 m/s can reach 10^6 K/s and decreases to 10^4 K/s at ~10 µm away from the wheel side, which is in good agreement with estimated values obtained by direct measurement in Al-Si [48] and Fe-Si-B systems [35]. Another strong evidence to support the inhomogeneous local cooling rate during melt spinning is the appearance of θ-Al_5Sm at the wheel side in Fig. 2. This phase was only observed from the Al-Sm STF samples before [13], which was prepared by condensation of metallic vapor through magnetron sputtering. The MG of STF should undergo a much higher cooling rate (estimated as ~ 10^9 K/s [49]) than the averaged cooling rate in melt spinning. Therefore, the formation of θ-Al_5Sm at the wheel side in the current MSR and previous magnetron sputtered thin-film suggests the θ-Al_5Sm phase is favored during devitrification of the Al-Sm amorphous ribbon prepared using a higher cooling rate.

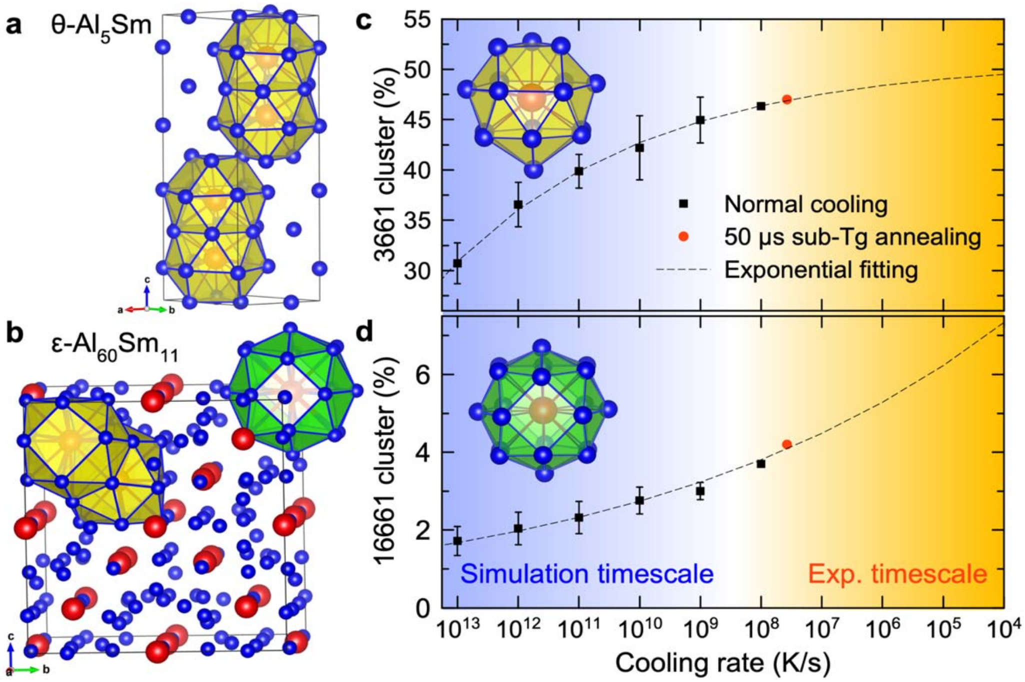

Fig. 4. The population of crystalline clusters as a function of cooling rates. (**a**) Crystal structures of θ-Al_5Sm and (**b**) ε-$Al_{60}Sm_{11}$. The 3661 and 16661-type clusters are highlighted with yellow and green, respectively. Red is Sm, and blue is Al. (**c**) The population of 3661 and (**d**) 16661-type clusters as a function of cooling rates. The inserts in the upper and lower panel show the 3661 and 16661 clusters, respectively. The dashed line indicates the exponential fittings.

3.2 Crystalline precursors in MG based on molecular dynamics simulations

The observed difference of devitrification between wheel- and free-side of melt-spun ribbon demonstrates that the cooling rate can tune the phase selection and crystallization pathway of Al-Sm MG from ε-Al_5Sm to θ-$Al_{60}Sm_{11}$. To further understand this scenario, molecular dynamics (MD) simulations are performed to investigate the precursor population change with cooling rates in the MG samples. While ε-$Al_{60}Sm_{11}$ and θ-Al_5Sm phases have very different crystallographic features, one can see similarities from atomic clusters. As shown in Fig. 4a and b, all Sm atoms in θ-Al_5Sm shows the adjacent "3661"-type clusters, which consists of a top triangular Al layer followed by two hexagonal Al layers and a bottom atom (see inset in Fig. 4c). ε-$Al_{60}Sm_{11}$ not only has 3661-type clusters but also presents a 16661-type cluster (inset in Fig. 4d), which consists of 20 Al coordinates, forming three hexagonal Al layers with two Al atoms at the top and bottom. The packing of these clusters fills 3D space in the two crystalline phases (see Fig.4 in Supplementary Materials (Ref. [])). The fact that 16661 clusters only present in ε-$Al_{60}Sm_{11}$ indicates that the 16661 clusters should be the critical precursor to control the phase selection between ε-$Al_{60}Sm_{11}$ and θ-Al_5Sm.

To understand the dependence of the 3661 and 16661 clusters on the cooling rate in the $Al_{90}Sm_{10}$ MG, we generate an MG model with uniform cooling simulation up to 10^8 K/s [50]. To reduce the gap between experimental and computational cooling rates, annealing simulation at a temperature below but close to the glass transition temperature (sub-T_g) is performed to achieve a more realistic atomistic MG model[41]. Thus, in addition to standard uniform cooling, sub-T_g annealing was performed to reach an effective cooling rate of about 4×10^7 K/s. With cluster alignment methods [51], the population of two types of clusters is shown as a function of the cooling rate in Fig. 4(c) and (d). The population of 3661 and 16661 clusters in the sub-T_g annealed sample are consistent with the dashed line trend established based on the uniformly cooled samples. Overall, the MD simulations show that the 3661-type cluster is dominant in the MG sample, while 16661 only shows a small population. When slowing down the cooling rate, the population of 3661 clusters starts to show a plateau, while the 16661 cluster population shows a large increase. Therefore, the main effect of slower cooling is to increase the 16661 cluster population. Since 16661 only exists in ε-$Al_{60}Sm_{11}$, the population of 16661 clusters is the rate-limiting factor controlling the formation of the ε-$Al_{60}Sm_{11}$ under the slower cooling.

From the viewpoint of atomic packing, as shown in Fig. 4, the 16661 cluster is composed of 20 neighbor atoms surrounding the center Sm atom, while 3661 has 16 neighbor atoms. Because the averaged Sm coordination number in the $Al_{90}Sm_{10}$ is ~16, 16661 is much rarer than 3661 in the glass and requires a much slower cooling rate to accumulate. Since 3661 clusters are always abundant in the glass regardless of cooling rates, θ-Al_5Sm can form even the glass was cooled at a higher cooling rate and not well relaxed. Therefore θ-Al_5Sm is observed in the STF and wheel side of MSR. However, ε-$Al_{60}Sm_{11}$ is unlikely to form unless the population of 16661 clusters reaches a critical value at a sufficiently slow cooling rate. These analyses demonstrate the population of 16661 clusters, controlled by the cooling rate, directly affects the phase selection of the AlSm MG in the devitrification.

The current observation can also be understood from the viewpoint of the temperature-time-transformation (TTT) diagram, which provides a framework to quantify the glass formation and crystallization. In a typical TTT diagram, at high cooling rates, the temperature-time trajectory cannot intersect the nose of the crystalline region (C-curve) so that it avoids the formation of the equilibrium crystalline phase and leads to a glass state. A recent study by Derlet and Maaß [52] revealed isotherm relaxation could drive the model binary glass towards amorphous crystalline nano-composite micro-structures, which locates in-between the monolithic glass state and equilibrium crystalline state on the TTT diagram. Our current observation of cooling-rate-dependent glass structure and devitrification pathways supports the existence of such intermediate amorphous states in the TTT diagram. Depending on the distance of temperature-time curve away from the nose point, different short or medium-range order could develop in the undercooling liquid or glass. These ordering eventually affect the devitrified phases and microstructures. Our findings further indicate the cooling process can greatly affect the intermediate states and their phase selection along the isotherm.

The shear stress between the supercooled liquid and rotating wheels is also an important factor to control the crystallization during the rapid quenching. F. Mura et al. [53] reported that the flow-induced nucleus straining lowers the nucleation rate by increasing the nucleation energy barrier. This mechanism could further reduce the nucleus at the wheel side. Therefore, the high cooling rate and shear stress at the wheel side can both stabilize the glass structures against devitrification.

3.3 Dependence of grain size on the distance to the wheel side

After understanding the cooling rate dependence of 16661 populations, we discuss the grain size profile of the ε-$Al_{60}Sm_{11}$ phase observed in Fig. 3b. In the current MG sample, the cooling rate is believed to be monotonously decreasing with the distance away from the wheel side, which directly correlates with the population of quenched-in 16661 nuclei [27].

Since a slower cooling rate leads to more 16661 clusters, as shown in Fig. 4(d), the number of ε-$Al_{60}Sm_{11}$ nuclei should increase from the wheel side region to the free side. Interestingly, the measured grain size given in Fig. 3b shows a non-monotonic dependence on the distance from the wheel side. This can be interpreted qualitatively by two kinetics at different stages of crystal growth. In the following, we set up a simplified model that captures the essential physics during the two stages of the growth, namely free expansion and coalescence, and demonstrate that through the competition of the different kinetics in these two growth stages, it is possible to produce the nonmonotonic grain size profile as observed in the experiments. During the early stage when a nucleus is fully embedded in the parent amorphous phase, the growth kinetics is controlled by the difference between the attachment and detachment rates at the interface [54], which results in a linear growth rate α: $dR/dt = \alpha$, where R is the average nuclei radius. During the second stage, when nuclei impinge on each other, the crystal growth is controlled by the migration through curvature-driven grain boundary motion [55]. Both Monte-Carlo simulations based on the Potts model and phase-field modeling [56] demonstrated that parabolic growth law ($R^2 \sim t$)) is satisfied in this scenario, or in the differential form: $dR/dt = \beta/R$ where β is a constant. We constructed the following model that captures the essence of the different kinetics in these two stages. That is, we assume the linear growth dominates when $t < t_0$, while the grain-boundary migration takes over when $t > t_0$. The rate equation for nuclei growth can then be written as

$$\frac{dR}{dt} = \begin{cases} \alpha \ (t < t_0) \\ \beta/R \ (t \geq t_0) \end{cases}. \tag{1}$$

Since the two parameters controlling the growth kinetics α and β have dimensions of [length][time]$^{-1}$ and [length]^2[time]$^{-1}$, respectively, β/α and β/α^2 give characteristic units for length and time, respectively. Assuming the grain-size measurement was taken well after t_0 for all regions across the sample, we plot the grain size at an arbitrary time instant $t = 6\beta/\alpha^2$ as a function of t_0 ranging from 0 to $2\beta/\alpha^2$ in Figure 5. As one can see, relatively large grains appear at both ends for different reasons: for large t_0, grains can experience unhindered growth in the amorphous background for a long period of time; while for small t_0, grains coalesce at relatively small sizes with high coalescence rates ($\propto 1/R$). Clearly, the larger the nuclei density is, the shorter time it takes for nuclei to interact, so one expects t_0 to decrease from the wheel side to the free side along the sample. Therefore, the model given in Eqn. (1) provides a qualitative match with the experimental measurements, as shown in Figure 3b. We note while the current model provides qualitative explanation on the grain size, a more sophisticated model which includes all the effect of cooling rate dependence and shear stress during the cooling process is still desired. We leave this for future study.

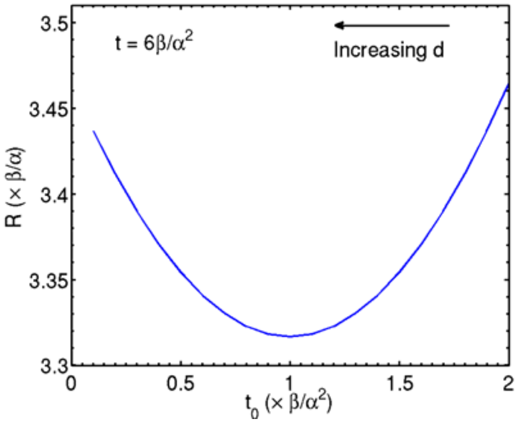

Fig. 5. Grain size at $t = 6\,\beta/\alpha^2$ as a function of t_0 according to the crystal growth model. The arrow indicates the direction of increasing distance (*d*) from the wheel side.

4. Conclusion

In summary, the devitrification process of Al-Sm MG synthesized by melt-spinning were systematically investigated using *in-situ* synchrotron X-ray scattering, associated with ex-situ TEM observations. *Ex-situ* microstructure observation reveals that the thin layer close to the wheel side shows a delayed crystallization and dramatically different phase selection and morphology compared to the area far from the wheel side. MD simulations quantitatively show the cooling rate dependence of nuclei density in amorphous states. It suggests the 16661 nuclei is the key factor in determining phase selection between ε-$Al_{60}Sm_{11}$ and θ-Al_5Sm. Cooling rate varying from the wheel- to free-side determines the density of quenched-in ε-$Al_{60}Sm_{11}$ nuclei, thus resulting in a different grain size evolution. These results suggest that the cooling rate can be an important processing condition to control the structure of the seemingly homogeneous MG and its crystallization pathways upon heating. Grain coalescence away from the wheel-side is regarded as the origin for coarse grain size, while fewer nucleation sites close to the wheel side is the major factor to determine the overall grain morphology. These findings provide direct proof to support the hereditary dependence of crystallization behavior on the liquid and glass states. The results emphasize the key factor of the cooling rate on determining the phase and microstructure evolution during the devitrification process. It indicates the local chemical and structural order can be sensitive to the processing and can greatly affect the properties of an alloy, which can be quite general in many MG systems. Therefore, our findings could help develop the strategy of microstructure design via quenched-in clusters with controlling the cooling process.

Acknowledgments

F.M. thanks Ryan T. Ott and Matthew F. Besser (Ames Laboratory, Iowa State University) for their support in the enlightening discussion. This work was supported by Ames Laboratory, the U.S. Department of Energy, Office of Science, Basic Energy Sciences, Materials Science and Engineering Division. Ames Laboratory is operated for the U.S. Department of Energy by Iowa State University under Contract No. DE-AC02-07CH11358. The use of the Advanced Photon Source was supported by the US Department of Energy, Office of Science, Office of Basic Energy Sciences, under Contract No. DE-AC02-06CH11357. D.S acknowledges the support from "The Pearl River Talent Program".

References

[1] Kelton and F. K., pergamon materials, 85 (2010).

[2] M. Wang, K. Zhang, Z. Li, Y. Liu, J. Schroers, M. D. Shattuck, and C. S. Ohern, Phys. Rev. E **91**, 032309 (2015).
[3] S. Lan, Z. Wu, X. Wei, J. Zhou, Z. P. Lu, J. Neuefeind, and X. Wang, Acta Mater. **149**, 108 (2018).
[4] K. F. Kelton, Phys Rev B Solid State **45**, 75 (1991).
[5] F. Meng, S. Zhou, R. Ott, M. Kramer, and R. Napolitano, Materialia, 100595 (2020).
[6] N. Wang, Y. E. Kalay, and R. Trivedi, Acta Mater. **59**, 6604 (2011).
[7] J. Zhou, Y. Yang, Y. Yang, D. Kim, A. Yuan, X. Tian, C. Ophus, F. Sun, A. K. Schmid, and M. Nathanson, Nature **570**, 500 (2019).
[8] Z. Wang, F. Wang, Y. Peng, and Y. Han, Nature Communications **6**, 6942 (2015).
[9] D. Gebauer, A. Volkel, and H. Colfen, Science **322**, 1819 (2008).
[10] D. Gebauer, M. Kellermeier, J. D. Gale, L. Bergstrom, and H. Colfen, Chem. Soc. Rev. **43**, 2348 (2014).
[11] V. N. Novikov and A. P. Sokolov, Nature **431**, 961 (2004).
[12] S. Lan, C. Guo, W. Zhou, Y. Ren, J. Almer, C. Pei, H. Hahn, C. T. Liu, T. Feng, and X. Wang, Communications in Physics **2**, 1 (2019).
[13] Z. Ye, F. Zhang, Y. Sun, M. I. Mendelev, R. T. Ott, E. Park, M. F. Besser, M. J. Kramer, Z. J. Ding, C. Z. Wang, and K. M. Ho, Appl. Phys. Lett. **106**, 101903 (2015).
[14] Z. Ye, F. Zhang, Y. Sun, M. C. Nguyen, S. H. Zhou, L. Zhou, F. Meng, R. T. Ott, E. Park, and M. F. Besser, Phys. Rev. Mater. **1**, 055601 (2017).
[15] R. Busch, S. Schneider, A. Peker, and W. Johnson, Appl. Phys. Lett. **67**, 1544 (1995).
[16] J. C. Qiao, Q. Wang, J. M. Pelletier, H. Kato, R. Casalini, D. Crespo, E. Pineda, Y. Yao, and Y. Yang, Prog. Mater Sci. **104**, 250 (2019).
[17] T. S. Ingebrigtsen, J. C. Dyre, T. B. Schroder, and C. P. Royall, Physical Review X **9**, 031016 (2019).
[18] K. Kelton, Philos. Mag. Lett. **77**, 337 (1998).
[19] H. W. Sheng, W. K. Luo, F. M. Alamgir, J. Bai, and E. Ma, Nature **439**, 419 (2006).
[20] A. Hirata, P. Guan, T. Fujita, Y. Hirotsu, A. Inoue, A. R. Yavari, T. Sakurai, and M. Chen, Nat. Mater. **10**, 28 (2011).
[21] D. Z. Chen, C. Y. Shi, Q. An, Q. Zeng, W. L. Mao, W. A. Goddard, and J. R. Greer, Science **349**, 1306 (2015).
[22] J. Ding and E. Ma, Npj Computational Mathematics **3** (2017).
[23] Z. Zhang and W. Kob, Proceedings of the National academy of Sciences of the United States of America (2020).
[24] L. Xing, T. Hufnagel, J. Eckert, W. Löser, and L. Schultz, Appl. Phys. Lett. **77**, 1970 (2000).
[25] L. Xing, Y. Shen, and K. Kelton, Appl. Phys. Lett. **81**, 3371 (2002).
[26] S. K. Das, J. H. Perepezko, R. I. Wu, and G. Wilde, Materials Science and Engineering: A **304-306**, 159 (2001).
[27] J. Holzer and K. Kelton, Acta Metall. Mater. **39**, 1833 (1991).
[28] C. Desgranges and J. Delhommelle, Phys. Rev. Lett. **120**, 115701.1 (2018).
[29] J. Russo, F. Romano, and H. Tanaka, Physical Review X **8**, 021040 (2018).
[30] L. Battezzati, M. Baricco, P. Schumacher, W. C. Shih, and A. L. Greer, Materials Science and Engineering: A **179-180**, 600 (1994).
[31] G. Wilde, H. Sieber, and J. H. Perepezko, Scr. Mater. **40**, 779 (1999).
[32] Y. Sun, F. Zhang, Z. Ye, Y. Zhang, X. Fang, Z. Ding, C. Wang, M. I. Mendelev, R. T. Ott, and M. J. Kramer, Sci. Rep. **6**, 23734 (2016).
[33] L. Wang, J. J. Hoyt, N. Wang, N. Provatas, and C. W. Sinclair, Nature communications **11**, 1 (2020).
[34]
[35] M. J. Kramer, H. Mecco, K. W. Dennis, E. Vargonova, R. W. Mccallum, and R. E. Napolitano, J. Non-Cryst. Solids **353**, 3633 (2007).
[36] W. M. Brown, P. Wang, S. J. Plimpton, and A. N. Tharrington, Comput. Phys. Commun. **182**, 898 (2011).
[37] W. M. Brown, A. Kohlmeyer, S. J. Plimpton, and A. N. Tharrington, Comput. Phys. Commun. **183**, 449 (2012).
[38] W. M. Brown and M. Yamada, Comput. Phys. Commun. **184**, 2785 (2013).

[39] M. Mendelev, F. Zhang, Z. Ye, Y. Sun, M. Nguyen, S. Wilson, C. Wang, and K. Ho, Modell. Simul. Mater. Sci. Eng. **23**, 045013 (2015).
[40] M. Finnis and J. Sinclair, Philos. Mag. A **50**, 45 (1984).
[41] F. Zhang, M. I. Mendelev, Y. Zhang, C.-Z. Wang, M. J. Kramer, and K.-M. Ho, Appl. Phys. Lett. **104**, 061905 (2014).
[42] Y. Sun, Y. Zhang, F. Zhang, Z. Ye, Z. Ding, C. Z. Wang, and K. M. Ho, J. Appl. Phys. **120**, 015901 (2016).
[43] L. Zhou, F. Meng, S. Zhou, K. Sun, T. Kim, R. Ott, R. Napolitano, and M. J. Kramer, Acta Materialia (2018).
[44] Y. E. Kalay, C. Yeager, L. S. Chumbley, M. J. Kramer, and I. E. Anderson, J. Non-Cryst. Solids **356**, 1416 (2010).
[45] L. Yang, F. Zhang, F.-Q. Meng, L. Zhou, Y. Sun, X. Zhao, Z. Ye, M. J. Kramer, C.-Z. Wang, and K.-M. Ho, Acta Mater. **156**, 97 (2018).
[46] B. Karpe, B. Kosec, and M. Bizjak, Journal for achievement in materials and manufacturing engineering, International OCSCO world press **51**, 59 (2012).
[47] M. Sowjanya and T. K. K. Reddy, J. Mater. Process. Technol. **214**, 1861 (2014).
[48] C. Xu, H. Wang, F. Qiu, Y. Yang, and Q. Jiang, Materials Science and Engineering: A **417**, 275 (2006).
[49] J. H. He, H. W. Sheng, P. J. Schilling, C. L. Chien, and E. J. P. R. L. Ma, Phys. Rev. Lett. **86**, 2826 (2001).
[50] Y. Sun, S. Peng, Q. Yang, F. Zhang, M. Yang, C. Wang, K. Ho, and H. B. Yu, Phys. Rev. Lett. **123**, 105701 (2019).
[51] C. Wang, Y. Yao, K. Ho, and Z. J. Ding, Phys. Rev. B **82** (2010).
[52] P. M. D. A and R. M. B, J. Alloys Compd. **821**.
[53] F. Mura and A. Zaccone, Phys. Rev. E **93**, 042803 (2016).
[54] J. J. De Yoreo and P. G. Vekilov, Reviews in Mineralogy & Geochemistry **54**, 57 (2003).
[55] A. Vuppuluri and S. J. P. M. L. Vedantam, **96**, 1 (2016).
[56] V. Tikare, E. A. Holm, D. Fan, and L. Chen, Acta Mater. **47**, 363 (1998).